TRANSACTIONS ON EMERGING TELECOMMUNICATIONS TECHNOLOGIES
Trans. Emerging Tel. Tech. 2012; **23**:764–776
Published online 10 July 2012 in Wiley Online Library (wileyonlinelibrary.com). DOI: 10.1002/ett.2555

RESEARCH ARTICLE

Sparse channel estimation for wavelet-based underwater acoustic communications

Chenhao Qi* and Lenan Wu

Key Laboratory of Underwater Acoustic Signal Processing of Ministry of Education, School of Information Science and Engineering, Southeast University, Nanjing 210096, China

ABSTRACT

In this paper, concerning underwater acoustic (UWA) communications, we propose a wavelet filter bank system as the extension of orthogonal frequency-division multiplexing system. We exploit the convolutional structure of a UWA channel and formulate the pilot-assisted channel estimation as a sparse recovery problem. Then, we investigate the restricted isometry property of the measurement matrix via eigenvalue analysis and Gershgorin circle theorem. The sparse recovery problem is proven to satisfy the restricted isometry property. Moreover, we also propose a low-complexity complex-field homotopy algorithm for sparse channel estimation, regarding the fact that the channel taps of each path are usually complex valued in practice. Simulation results show that the wavelet filter bank system achieves more accurate UWA channel estimation performance than orthogonal frequency-division multiplexing system under the same conditions of bandwidth, duration, data rate and channel profile. The proposed complex homotopy algorithm outperforms orthogonal matching pursuit (OMP) and stagewise OMP in both systems, whereas its computational complexity is similar to OMP. Copyright © 2012 John Wiley & Sons, Ltd.

***Correspondence**
Chenhao Qi, School of Information Science and Engineering, Southeast University, Nanjing 210096, China.
E-mail: qch@seu.edu.cn

Received 13 February 2012; Revised 27 May 2012; Accepted 30 May 2012

1. INTRODUCTION

Underwater acoustic (UWA) communications are of increasing interest in the study of high-rate and reliable digital communications for submarines and various underwater vehicles as well as a wide variety of applications, that is, deep-sea fishing, oil exploration, wildlife tracking and environmental monitoring. However, three main challenges exist in the development of UWA communications. The first one is the scarce frequency resource. UWA signals experience considerable attenuation at high frequency range because the water absorption grows rapidly with the distance and the carrier frequency. Meanwhile, regarding the severe UWA channel noise at low frequency, the band for UWA communications is only available at medium frequency and therefore is very limited. For example, to communicate at the distance of 100 k, only 1-kHz bandwidth is available [1]. The second challenge is the Doppler effect. Because the bandwidth is comparable with the carrier frequency in UWA communications, it is a typical wideband system where the Doppler shift cannot be regarded as the same for the whole band. Moreover, considering the fact that the speed of sound, that is, 1500 m/s in the seawater, is very slow compared with the speed of electromagnetic waves in the air, any relative motion between the transmitter and the receiver will cause severe Doppler distortion. The last challenge is the abundant multipath propagation. In addition to the direct path, the acoustic signal propagates via multiple reflections from the surface, bottom and other objects, as shown in Figure 1. The large delay spread leads to strong frequency selectivity that may be highly time varying. The inter-symbol interference (ISI) may spread over several hundreds of symbol periods, which brings heavy burden to the front-end preprocessing for combatting the channel effect at the receiver.

The earlier UWA systems use frequency shift keying to modulate signal into discrete tones with guard time and guard bands. Although these systems carefully avoid ISI, making them easy for implementation, the data rates are only around 1 kb/s. Then, coherent demodulation technique increases the data rate and spectral efficiency by adaptive phase tracking and equalisations, which demonstrates its significant improvement over noncoherent methods and achieves data rate of 10 kb/s in short-range, shallow-water UWA channels [2]. Recently, orthogonal frequency-division multiplexing (OFDM), which has

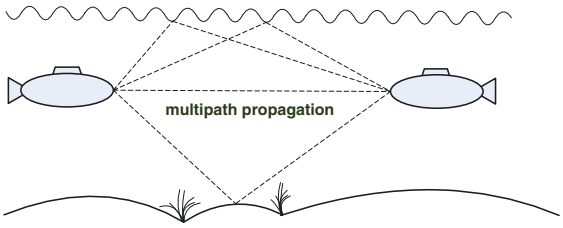

Figure 1. Multipath propagation of underwater acoustic communications.

prevailed in wireless radio systems, has also been applied to UWA communications [3, 4]. OFDM transforms the frequency-selective channel into several parallel flat-fading narrowband subchannels, where each subband only needs a single-tap equaliser. Therefore, the high complexity associated with the long decision feedback equaliser in single-carrier systems is mitigated. More recently, the wavelet has been applied for UWA communications because of its inherent advantage of filtering out narrowband interference by wavelet denoising [5, 6]. Wavelet-based Doppler compensation can be equally converted into the diversity combination for the optimum receiver design [7]. OFDM requires a guard interval, such as cyclic prefix and zero padding, to combat inter-channel interference (ICI) and ISI caused by channel multipath. The overhead of the guard interval is saved in wavelet systems, especially for UWA channels whose delay spread is usually very large. Additionally, OFDM employs rectangular or other types of window to suppress side lopes of power spectrum, which produces ICI and ISI that damage the orthogonality of subcarriers [8–10]. It is demonstrated in [11] that lower ICI and ISI than OFDM can be achieved in wavelet systems. In particular, a wavelet filter bank system can be regarded as the extension of an OFDM system where the Fourier basis is employed instead of the wavelet basis [12].

Nevertheless, one of the largest barriers blocking UWA communications is the UWA channel distortion. Compared with single-carrier systems, OFDM estimates the channel before making the one-tap channel equalisation, which substantially reduces the receiver's complexity. And with the further combination of the recently emerged compressed sensing (CS) techniques [13–15], UWA channel estimation is much more simplified. The channel impulse response (CIR) can be reconstructed through CS algorithms because the UWA channel is usually dominated by a small number of significant paths, resulting in a sufficient sparse CIR [1]. This topic is currently undergoing explosive discussions [16, 17]. Many CS algorithms including matching pursuit (MP), orthogonal MP (OMP) and basis pursuit (BP) have been applied for UWA OFDM channel estimation [18–20]. Specifically, BP is shown to outperform OMP [21]. In [22], three BP algorithms including ℓ_1-LS, YALL1 and SpaRSA are compared. However, the complexity of BP algorithms is much higher than that of OMP. For UWA channels where the estimates have to be frequently updated, applying BP for real-time channel estimation is computationally very expensive. So it is necessary to explore lower-complexity CS algorithms.

In this paper, we first construct a wavelet filter bank system as the extension of OFDM system for UWA communications. We exploit the convolutional structure and formulate the pilot-assisted UWA channel estimation as a sparse recovery problem. Then, we investigate the restricted isometry property (RIP) of the measurement matrix via eigenvalue analysis and Gershgorin circle theorem. We also propose a low-complexity complex-field homotopy algorithm for sparse channel estimation regarding the fact that in practice the channel taps of each path are usually complex valued. Additionally, we also compare the channel estimation performance for the wavelet filter bank and OFDM systems in terms of mean square error (MSE) and bit error rate (BER).

The remainder of the paper is organised as follows. Section 2 constructs a wavelet filter bank system and formulates the UWA channel estimation as a sparse recovery problem. Section 3 investigates the RIP through eigenvalue analysis and Gershgorin circle theorem. In Section 4, a low-complexity complex-field homotopy algorithm is proposed for sparse channel estimation. Simulation results are presented in Section 5, and finally, Section 6 concludes this paper.

The notation used in this paper is according to the convention. Symbols for matrices (upper case) and vectors (lower case) are in boldface. $(\cdot)^{\mathrm{T}}$, $(\cdot)^{\mathrm{H}}$, $|\cdot|$, $\|\cdot\|_1$ $\|\cdot\|_2$, $\lfloor\cdot\rfloor$, $\mathbb{C}$, $\mathbb{R}$, diag$\{\cdot\}$, $\boldsymbol{I}_L$, $\boldsymbol{0}_{M\times N}$, $\Re$, $\Im$ and $\mathcal{CN}$ denote transpose, conjugate transpose (Hermitian), absolute value, ℓ_1-norm, ℓ_2-norm, the floor, the set of complex number, the set of real number, the diagonal matrix, the identity matrix with dimension L, the M by N zero matrix, the real part, the imaginary part and the complex Gaussian distribution, respectively. $\mathcal{O}(\cdot)$ means the order. $\hat{\phi}$ denotes the estimate of the parameter of interest ϕ.

2. PROBLEM FORMULATION

We consider the UWA channel that has a time-varying multipath CIR as

$$h(\tau,t)=\sum_{i=1}^{S}\xi_i(t)\delta(\tau-\tau_i(t)) \tag{1}$$

where S, $\xi_i(t)$ and $\tau_i(t)$ are the number of total path, the ith time-varying path attenuation and path delay, respectively. We adopt two assumptions as follows:

(1) All paths have the same Doppler scaling factor $\alpha(t)$ such that

$$\tau_i(t)\approx\tau_i-\alpha(t)t \tag{2}$$

which supposes that the dominant Doppler shift is caused by the relative movement between the transmitter and the receiver [3].

(2) $\xi_i(t)$, $\tau_i(t)$ and $\alpha(t)$ are constant over each data block, which contains several data symbols or training symbols. We represent them as ξ_i, τ_i and α, respectively. This assumption is reasonable because the UWA channel coherence time is usually on the order of seconds [3], whereas the duration of each data block is no more than hundreds of milliseconds. In fact, this assumption is common when we deal with time-varying channels.

Let $e(t) = \mathrm{Re}\{s(t)e^{j2\pi f_c t}\}$ denote the transmitted signal in passband, where f_c is the carrier frequency and $s(t)$ is the baseband signal. Then, the received passband signal is

$$\begin{aligned} z(t) &= \int_{-\infty}^{\infty} h(\tau,t)e(t-\tau)\mathrm{d}\tau + \eta(t) \\ &= \mathrm{Re}\left\{\sum_{i=1}^{S}\xi_i(t)s\left(t-\tau_i(t)\right)e^{j2\pi f_c(t-\tau_i(t))}\right\} \\ &\quad + \eta(t) \\ &= \mathrm{Re}\left\{\sum_{i=1}^{S}\xi_i(t)s\left(\left(1+\alpha(t)\right)t-\tau_i\right)\right. \\ &\quad \left.\cdot e^{j2\pi f_c((1+\alpha(t))t-\tau_i)}\right\} + \eta(t) \end{aligned} \tag{3}$$

where $\eta(t)$ is the additive Gaussian noise. During each data block that $\xi_i(t)$, $\tau_i(t)$ and $\alpha(t)$ are constant, we have

$$\begin{aligned} \tilde{z}(t) = \mathrm{Re}&\left\{\sum_{i=1}^{S}\xi_i s\left((1+\alpha)t-\tau_i\right)\right. \\ &\left.\cdot e^{j2\pi f_c((1+\alpha)t-\tau_i)}\right\} + \eta(t) \end{aligned} \tag{4}$$

where we notice that the received signal is scaled by $1/(1+\alpha)$ in duration. Because the bandwidth is comparable with the carrier frequency in UWA communications, the Doppler shift $e^{j2\pi f_c\alpha t}$ cannot be regarded as uniform for the whole bandwidth.

We directly sample the received passband signal without down-conversion because the frequency range used for UWA communications is usually in tens of thousands of hertz, which is more convenient for implementation in software-defined radio. To estimate the resampling factor, we design each data block containing one preamble and one postamble. In [23], a structure of preamble is proposed where it consists of two identical OFDM symbols and one cyclic prefix. And correspondingly, a bank of self-correlators is employed for the receiver with each of the self-correlators matched to a different duration. Then, the estimated length of data block $\hat{T}_{rx}$ equals the branch that has the maximum correlation with the received signal. Because the length of transmitted data block T_{tx} is explicitly known beforehand, the estimated Doppler scaling factor is

$$\hat{\alpha} = \frac{T_{tx}}{\hat{T}_{rx}} - 1 \tag{5}$$

However, the shortcoming of this approach is that the estimation accuracy relies on the number of self-correlators. Therefore, in this paper, we design the preamble and the postamble to be linear-frequency-modulated signals. By cross-correlating the received signal with the known preamble and postamble, the receiver estimates the length of each data block and figures out $\hat{\alpha}$, which is more flexible than using a bank of self-correlators.

We resample the received signal $\tilde{z}$ in Equation (4) as

$$\begin{aligned} r(t) &= \tilde{r}\left(\frac{t}{1+\hat{\alpha}}\right) \\ &= \mathrm{Re}\left\{\sum_{i=1}^{S}\xi_i s\left(\frac{1+\alpha}{1+\hat{\alpha}}t-\tau_i\right)\right. \\ &\quad \left.\cdot e^{j2\pi f_c\left(\frac{1+\alpha}{1+\hat{\alpha}}t-\tau_i\right)}\right\} + \tilde{\eta}(t) \end{aligned} \tag{6}$$

where $\tilde{\eta}(t)$ is the resampling result of $\eta(t)$. Then, the equivalent received baseband signal is

$$\tilde{r}(t) = \sum_{i=1}^{S}\xi_i s\left(\frac{1+\alpha}{1+\hat{\alpha}}t-\tau_i\right)e^{j2\pi f_c\left(\frac{\alpha-\hat{\alpha}}{1+\hat{\alpha}}t-\tau_i\right)} + \eta_B(t) \tag{7}$$

where $\eta_B(t)$ is the equivalent baseband noise. Although we intend to make $(1+\alpha)$ as close to $(1+\hat{\alpha})$ as possible, there is a residual carrier frequency offset [24] defined as

$$f_o = \left(\frac{\alpha-\hat{\alpha}}{1+\hat{\alpha}}\right)f_c \tag{8}$$

which can be viewed as uniform for the whole band. Hence, a wideband system is converted into a narrowband system with frequency-independent carrier frequency offset, which can be conveniently compensated in the wavelet filter bank systems [25].

According to filter bank theories in wavelet, the scaling function and the wavelet function can be considered as a low-pass filter and a high-pass filter, respectively. Figure 2 gives a block diagram of a wavelet filter bank system. The serial data stream $x(n)$ is first converted into M parallel multirate data streams, $x_0(n), x_1(n), \ldots, x_{M-1}(n)$, where

$$x_i(n) = \begin{cases} x(2^{i+1}\cdot n - 2^i), & i = 0,1,\ldots,M-2 \\ x(2^{M-1}\cdot n - 2^{M-1}), & i = M-1 \end{cases} \tag{9}$$

Then, they pass through a bank of reconstruction wavelet filters with each filter comprising an upsampling operation $\uparrow n_i$ $(i = 0,1,\ldots,M-1)$ and a filtering operation $f_i(n)$ $(i = 0,1,\ldots,M-1)$. The output of every branch is combined together, denoted as $s(n)$. Then, $s(n)$ is sent into the UWA channel. At the receiver, $r(n)$ is first inputted into a bank of decomposition wavelet filters with each filter comprising a digital filtering operation $g_i(n)$ $(i = 0,1,\ldots,M-1)$ and a downsampling operation $\downarrow n_i$ $(i = 0,1,\ldots,M-1)$. After that, the parallel data streams are converted into a serial data stream $y(n)$.

Trans. Emerging Tel. Tech. **23**:764–776 (2012)
DOI: 10.1002/ett

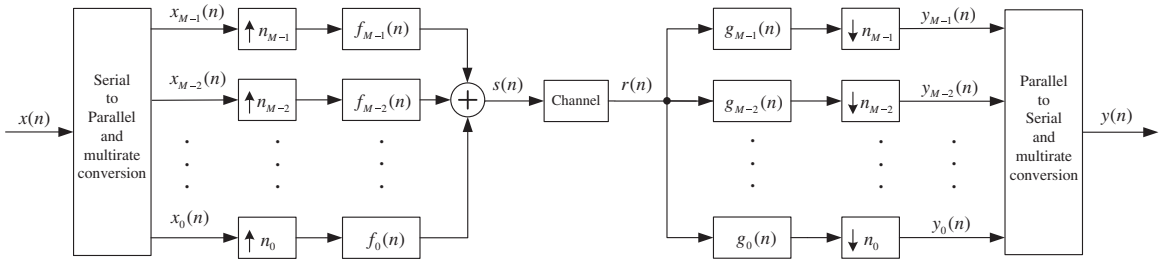

Figure 2. Wavelet filter bank system.

For a Haar wavelet, the scaling and wavelet functions can be written as

$$p(n) = \frac{1}{\sqrt{2}}\delta(n) + \frac{1}{\sqrt{2}}\delta(n-1) \tag{10}$$

and

$$q(n) = \frac{1}{\sqrt{2}}\delta(n) - \frac{1}{\sqrt{2}}\delta(n-1) \tag{11}$$

respectively. After cascade filter conversion and Z-transform, we have

$$n_i = \begin{cases} 2^{i+1}, & i = 0, 1, \ldots, M-2 \\ 2^{M-1}, & i = M-1 \end{cases} \tag{12}$$

and

$$f_i(z) = \begin{cases} \prod_{k=0}^{M-1} p(z^{2^k}), & i = M-1 \\ q(z^{2^i}) \prod_{k=0}^{i-1} p(z^{2^k}), & i = 1, \ldots, M-2 \\ q(z), & i = 0 \end{cases} \tag{13}$$

where $f_i(z)$ is the Z-transform of $f_i(n)$, denoted as

$$f_i(z) = \sum_{n=-\infty}^{+\infty} f_i(n) z^{-n} \tag{14}$$

Therefore,

$$\begin{aligned} s(n) &= \sum_{i=0}^{M-1} \sum_{k=0}^{\infty} x_i(k) f_i(n - 2^{i+1}k) \\ &= \sum_{k=0}^{\infty} \Big[x(2^{M-1} \cdot k - 2^{M-1}) \\ &\quad + \sum_{i=0}^{M-2} x(2^{i+1} \cdot k - 2^i) \Big] f_i(n - 2^{i+1}k) \end{aligned} \tag{15}$$

Now, we can formulate the received signal $r(n)$ as the discrete-time convolution from $s(n)$ and $h(n)$, which is denoted as

$$r(n) = s(n) * h(n) + \eta(n) \tag{16}$$

where $\eta(n)$ is the sample of additive white Gaussian noise. Let L denote the length of $h(n)$ and suppose the training sequence to be $\{s(n), n = 0, 1, \ldots, N_\mathrm{T} - 1\}$ $(N_\mathrm{T} > L)$. The resulting input–output relation of Equation (16) can be represented as a matrix–vector product

$$\tilde{\boldsymbol{r}} = \tilde{\boldsymbol{A}}\boldsymbol{h} + \tilde{\boldsymbol{\eta}} \tag{17}$$

where $\tilde{\boldsymbol{r}} = [r(0), r(1), \cdots, r(N_\mathrm{T}-1)]^\mathrm{T}$, $\boldsymbol{h} = [h(0), h(1), \cdots, h(L-1)]^\mathrm{T}$, $\tilde{\boldsymbol{\eta}} = [\eta(0), \eta(1), \cdots, \eta(N_\mathrm{T}-1)]^\mathrm{T} \sim \mathcal{CN}(\boldsymbol{0}, \sigma_\eta^2 \boldsymbol{I}_{N_\mathrm{T}})$ is a noise vector with each component to be an additive white Gaussian noise sample and

$$\tilde{\boldsymbol{A}} = \begin{bmatrix} s(0) & s(-1) & \cdots & s(-L+1) \\ s(1) & s(0) & \cdots & s(-L+2) \\ \vdots & \vdots & \ddots & \vdots \\ s(N_\mathrm{T}-1) & s(N_\mathrm{T}-2) & \cdots & s(N_\mathrm{T}-L) \end{bmatrix} \tag{18}$$

contains the known training sequences $\{s(n), n = 0, 1, \ldots, N_\mathrm{T}-1\}$ as well as unknown sequences $\{s(n), n = -L+1, -L+2, \ldots, -1\}$ that are located in the upper-right triangular area of $\tilde{\boldsymbol{A}}$. The unknown sequences can be some data symbols or null symbols that are unpredicted at the receiver. Therefore, we cannot directly use $\tilde{\boldsymbol{A}}$ for channel estimation. Instead, we have to use a submatrix

$$\boldsymbol{A} = \begin{bmatrix} s(L-1) & s(L-2) & \cdots & s(0) \\ s(L) & s(L-1) & \cdots & s(1) \\ \vdots & \vdots & \ddots & \vdots \\ s(N_\mathrm{T}-1) & s(N_\mathrm{T}-2) & \cdots & s(N_\mathrm{T}-L) \end{bmatrix} \tag{19}$$

of $\tilde{\boldsymbol{A}}$ for channel estimation. We observe that all components of $\boldsymbol{A}$ are known training symbols from $\{s(n), n = 0, 1, \ldots, N_\mathrm{T}-1\}$. The dimension of $\tilde{\boldsymbol{A}}$ and $\boldsymbol{A}$ are N_T by L and $(N_T - L + 1)$ by L, respectively. Then, Equation (17) is reformulated as

$$\boldsymbol{r} = \boldsymbol{A}\boldsymbol{h} + \boldsymbol{\eta} \tag{20}$$

where $\boldsymbol{r} = [r(L-1), r(L), \ldots, r(N_\mathrm{T}-1)]^\mathrm{T}$, $\boldsymbol{\eta} = [\eta(L-1), \eta(L), \ldots, \eta(N_\mathrm{T}-1)]^\mathrm{T}$. If $N_\mathrm{T} \geqslant 2L-1$, Equation (20) is an over-determined problem and least squares (LS) can be applied. However, we are more interested in

the under-determined case where $L \leqslant N_{\mathrm{T}} < 2L-1$ and the rows of $\boldsymbol{A}$ are less than its columns. In this case, only a small number of training sequence are required, which indicates the improvement in the data rate and spectrum efficiency. In combination with the recently emerged CS techniques, Equation (20) is undergoing extensive discussions on the sparse recovery performance of $\boldsymbol{h}$ from the measurement $\boldsymbol{r}$ and the measurement matrix $\boldsymbol{A}$. So in the following section, we investigate the RIP of $\boldsymbol{A}$.

Additionally, we also observed from Equation (20) that if $N_{\mathrm{T}} < L$, each row of Equation (17) contains unknown data symbols as well as known training symbols. The channel can only be estimated with the assistance of perfect symbol demodulation in an iterative manner, which is out of the scale of this work.

3. RESTRICTED ISOMETRY PROPERTY

Recent advances in CS show that $\boldsymbol{h}$ in Equation (20) can be recovered from $\boldsymbol{r}$ with high accuracy when $\boldsymbol{A}$ satisfies RIP [26].

Definition. *$\boldsymbol{A} \in \mathbb{R}^{m\times n}$ satisfies RIP if*

$$(1-\delta)\|\boldsymbol{h}\|_2^2 \leqslant \|\boldsymbol{A}\boldsymbol{h}\|_2^2 \leqslant (1+\delta)\|\boldsymbol{h}\|_2^2 \tag{21}$$

holds for all S-sparse vectors $\boldsymbol{h} \in \mathbb{R}^n$ ($\|\boldsymbol{h}\|_0 \leqslant S$).

It can be easily obtained from Equation (21) that

$$\begin{aligned}&(1-\delta)\|\boldsymbol{h}\|_2^2 \leqslant \lambda_{\min}\|\boldsymbol{h}\|_2^2\\ &\leqslant \|\boldsymbol{A}\boldsymbol{h}\|_2^2 \leqslant \lambda_{\max}\|\boldsymbol{h}\|_2^2 \leqslant (1+\delta)\|\boldsymbol{h}\|_2^2\end{aligned} \tag{22}$$

where $\lambda_{\min}$ and $\lambda_{\max}$ denote the minimum and maximum eigenvalues of $\boldsymbol{A}^{\mathrm{T}}\boldsymbol{A}$, respectively. Then, this sufficient condition for RIP is simplified as

$$1-\delta \leqslant \lambda_{\min} \leqslant \lambda_{\max} \leqslant 1+\delta \tag{23}$$

For example, if $\delta = 0.01$, then we have $0.99 \leqslant \lambda_{\min} \leqslant \lambda_{\max} \leqslant 1.01$, which implies that all the eigenvalues are distributed in a small circular area near the surface of a unit sphere.

Here, we start with the discussion on the RIP condition of $\boldsymbol{A}$ in Equation (20) before applying CS algorithms for the wavelet filter bank system. The Toeplitz CS matrices have been studied in [27]. However, here, we treat it in a simplified approach. First, we normalise $\boldsymbol{A}$ so that each column of $\boldsymbol{A}$ is normalised to 1. We have

$$\boldsymbol{A} = \boldsymbol{X}\boldsymbol{D} \tag{24}$$

where

$$\boldsymbol{D} = \mathrm{diag}\{\kappa_1, \kappa_2, \ldots, \kappa_L\} \tag{25}$$

is a diagonal matrix with each diagonal component as a normalised coefficient and

$$\boldsymbol{X} = \begin{bmatrix} \frac{s(L-1)}{\kappa_1} & \frac{s(L-2)}{\kappa_2} & \cdots & \frac{s(0)}{\kappa_L} \\ \frac{s(L)}{\kappa_1} & \frac{s(L-1)}{\kappa_2} & \cdots & \frac{s(1)}{\kappa_L} \\ \vdots & \vdots & \ddots & \vdots \\ \frac{s(N_{\mathrm{T}}-1)}{\kappa_1} & \frac{s(N_{\mathrm{T}}-2)}{\kappa_2} & \cdots & \frac{s(N_{\mathrm{T}}-L)}{\kappa_L} \end{bmatrix} \tag{26}$$

is an ℓ_2-normalised matrix. $\boldsymbol{X} \in \mathbb{R}^{N\times L}$ where $N = N_T - L + 1$. In this way, we guarantee that every diagonal component of $\boldsymbol{V} = \boldsymbol{X}^{\mathrm{T}}\boldsymbol{X}$ is 1. Let $\boldsymbol{V}_{i,j}$ represent the component in the ith row, jth column of $\boldsymbol{V}$. We have

$$\left\{\boldsymbol{V}_{i,i} = 1 \mid i \in \{1, 2, \ldots, L\}\right\} \tag{27}$$

Supposing

$$\tilde{\boldsymbol{h}} = \boldsymbol{D}\boldsymbol{h} \tag{28}$$

we reformulate Equation (20) as

$$\boldsymbol{r} = \boldsymbol{X}\tilde{\boldsymbol{h}} + \boldsymbol{\eta} \tag{29}$$

After $\tilde{\boldsymbol{h}}$ is reconstructed, we can obtain $\boldsymbol{h}$ by

$$\boldsymbol{h} = \boldsymbol{D}^{-1}\tilde{\boldsymbol{h}} \tag{30}$$

It is observed that each off-diagonal component of $\boldsymbol{V}$ is the inner product of two different columns of $\boldsymbol{X}$, that is,

$$\begin{aligned}\boldsymbol{V}_{1,2} = &(s(L-2)s(L-1) + s(L-1)s(L)\\ &+ s(L)s(L+1) + s(L+1)s(L+2)\\ &+ \cdots + s(N_{\mathrm{T}}-3)s(N_{\mathrm{T}}-2)\\ &+ s(N_{\mathrm{T}}-2)s(N_{\mathrm{T}}-1))\ /\kappa_1\kappa_2\end{aligned} \tag{31}$$

It is possible to split the summation into two groups as

$$\begin{aligned}\boldsymbol{V}_{1,2} = &(s(L-2)s(L-1) + s(L)s(L+1) + \cdots\\ &+ s(N_{\mathrm{T}}-3)s(N_{\mathrm{T}}-2))\ /\kappa_1\kappa_2\\ &+ (s(L-1)s(L) + s(L+1)s(L+2)\\ &+ \cdots + s(N_{\mathrm{T}}-2)s(N_{\mathrm{T}}-1))\ /\kappa_1\kappa_2\end{aligned} \tag{32}$$

so that the items of the summation within each group are independent. We denote

$$\begin{aligned}\boldsymbol{V}_{1,2}^{(1)} = &s(L-2)s(L-1) + s(L)s(L+1) + \cdots\\ &+ s(N_{\mathrm{T}}-3)s(N_{\mathrm{T}}-2)\end{aligned} \tag{33}$$

and

$$\begin{aligned}\boldsymbol{V}_{1,2}^{(2)} = &s(L-1)s(L) + s(L+1)s(L+2) + \cdots\\ &+ s(N_{\mathrm{T}}-2)s(N_{\mathrm{T}}-1)\end{aligned} \tag{34}$$

Trans. Emerging Tel. Tech. **23**:764–776 (2012)
DOI: 10.1002/ett

Then,

$$\boldsymbol{V}_{1,2} = \left(\boldsymbol{V}_{1,2}^{(1)} + \boldsymbol{V}_{1,2}^{(2)} \right) / \kappa_1 \kappa_2 \tag{35}$$

Considering traditional modulation schemes such as phase shift keying and quadrature amplitude modulation, the constellation points are symmetrically distributed, and thus, the mean of these items is 0. Also notice that the amplitude of these points is finite because they usually lie within a circular or rectangular area. Then, we have

$$\mathbb{E}\{s(n)\} = 0 \tag{36}$$

and

$$|s(n)| \leqslant \kappa,\ n = 0, 1, \ldots, N_{\mathrm{T}} \tag{37}$$

According to Hoeffding's inequality, which states

$$\begin{aligned} &\Pr\left(\left| \sum_{i=1}^{k} \omega_i - \mathbb{E}\left\{ \sum_{i=1}^{k} \omega_i \right\} \right| \geqslant t \right) \\ &\leqslant 2\exp\left(-\frac{2t^2}{\sum_{i=1}^{k} (b_i - a_i)^2} \right) \end{aligned} \tag{38}$$

where

$$\{\, \omega_i \mid \omega_i \in [a_i, b_i], i \in \{1, 2, \ldots, k\} \,\} \tag{39}$$

are independent bounded random variables, we obtain

$$\Pr\left(\boldsymbol{V}_{1,2}^{(1)} \geqslant t \right) \leqslant 2\exp\left(-\frac{t^2}{(N_{\mathrm{T}} - L + 1)\kappa^4} \right) \tag{40}$$

and

$$\Pr\left(\boldsymbol{V}_{1,2}^{(2)} \geqslant t \right) \leqslant 2\exp\left(-\frac{t^2}{(N_{\mathrm{T}} - L + 1)\kappa^4} \right) \tag{41}$$

Therefore,

$$\begin{aligned} &\Pr\left(\left| \boldsymbol{V}_{1,2} \right| \geqslant \frac{\delta}{L-1} \right) \\ &\leqslant \Pr\left(\left| \boldsymbol{V}_{1,2}^{(1)} \right| \geqslant \frac{\delta\kappa_1\kappa_2}{2(L-1)} \ \text{ or } \ \left| \boldsymbol{V}_{1,2}^{(2)} \right| \geqslant \frac{\delta\kappa_1\kappa_2}{2(L-1)} \right) \\ &\leqslant 2\max\left\{ \Pr\left(\boldsymbol{V}_{1,2}^{(1)} \geqslant \frac{\delta\kappa_1\kappa_2}{2(L-1)} \right), \right. \\ &\qquad \left. \Pr\left(\boldsymbol{V}_{1,2}^{(2)} \geqslant \frac{\delta\kappa_1\kappa_2}{2(L-1)} \right) \right\} \\ &\leqslant 4\exp\left(-\frac{\delta^2\kappa_1^2\kappa_2^2}{4(N_{\mathrm{T}} - L + 1)(L-1)^2\kappa^4} \right) \end{aligned} \tag{42}$$

These steps can be conveniently extended to other off-diagonal elements of $\boldsymbol{V}$. According to the Gershgorin circle theorem, the eigenvalues of $\boldsymbol{V}$ all lie in L discs. The ith disc is centred at $\boldsymbol{V}_{i,i}$ with the radius as

$$r_{i,i} = \sum_{j=1, j\neq i}^{L} |\boldsymbol{V}_{i,j}| \tag{43}$$

It can be obtained from Equation (42) that

$$\begin{aligned} &\Pr\left(r_{i,i} \geqslant \delta \right) \\ &\leqslant \left[4\exp\left(-\frac{\delta^2\kappa_1^2\kappa_2^2}{4(N_{\mathrm{T}} - L + 1)(L-1)^2\kappa^4} \right) \right]^{L-1} \end{aligned} \tag{44}$$

which is the probability of the event that the eigenvalues of $\boldsymbol{V}$ lie outside $[1-\delta, 1+\delta]$. From Equation (23), we prove that $\boldsymbol{X}$ satisfies RIP with the probability greater than

$$1 - \left[4\exp\left(-\frac{\delta^2\kappa_1^2\kappa_2^2}{4(N_{\mathrm{T}} - L + 1)(L-1)^2\kappa^4} \right) \right]^{L-1} \tag{45}$$

4. COMPLEX HOMOTOPY

An S-sparse vector $\boldsymbol{h}$ in Equation (20) can be recovered from $\boldsymbol{r}$ and $\boldsymbol{A}$ by solving the ℓ_0-norm minimisation problem

$$\min_{\boldsymbol{h}} \|\boldsymbol{h}\|_0 \quad \text{s.t.} \quad \|\boldsymbol{r} - \boldsymbol{A}\boldsymbol{h}\|_2 \leqslant \sigma_\eta \tag{46}$$

where $\|\boldsymbol{h}\|_0$ counts the number of nonzero elements of $\boldsymbol{h}$. This is a nondeterministic polynomial-time hard combinatorial problem. However, it can be replaced by the following ℓ_1-norm optimisation problem [28]:

$$\min_{\boldsymbol{h}} \|\boldsymbol{h}\|_1 \quad \text{s.t.} \quad \|\boldsymbol{r} - \boldsymbol{A}\boldsymbol{h}\|_2 \leqslant \sigma_\eta \tag{47}$$

Currently, methods for solving Equation (47) can be roughly divided into two classes, including convex optimisation algorithms and greedy algorithms. The convex optimisation algorithms include ℓ_1-LS, YALL1, SpaRSA [29] and other optimisation solvers. However, these methods usually have high computational complexities. Greedy algorithms make a sequential locally optimal choice in an effort to determine a globally optimal solution and include MP, OMP [30], CoSaMP, subspace pursuit [31], gradient projection for sparse reconstruction [32] and homotopy [33]. Because frequent channel estimation is required in UWA communications, low-complexity greedy algorithms are much more preferred. Among the many greedy algorithms, CoSaMP and subspace pursuit require explicit knowledge of the sparsity, which means that we have to *a priori* know the number of the nonzero components of the CIR vector. However, this *a priori* knowledge is unavailable because the number of the multipath is usually unknown. MP and OMP have been extensively studied with their variants such as optimised OMP, backward-optimised OMP and stagewise OMP (StOMP) [34]. Although these variants may outperform OMP, their

complexities are much higher than OMP. In practice, OMP is still a reasonable trade-off between the performance and the complexity, especially for UWA channel estimation [17, 21, 22]. In [33] and [30], it has been shown that homotopy has the same order of complexity as OMP whereas its sparse recovery performance is as good as that obtained from convex optimisation.

Real-valued homotopy is proposed in [33] as a least angle regression [35] algorithm with the least absolute shrinkage and selection operator modifications. After greedy selection of the first column according to the maximum-inner-product rule and its addition to the current column selection as MP and OMP, homotopy steps forward until one column outside the selection appears to have the same inner product with the current residue as the columns inside the selection. Then, the column is selected, and a new step along an equiangular direction having the same inner product with all vectors in the selection is updated. The iteration is repeated until the stopping condition is satisfied. Unlike MP and OMP removing all the projective components at each iteration, homotopy only removes the part of it whose value actually equals the step length at each iteration. Once it eliminates the superiority of the maximal-inner-product column over other columns, homotopy fairly treats all the columns. Because the UWA channel is essentially sparse with complex-valued channel taps, we extend homotopy from the real field to the complex field before applying for UWA channel estimation.

Note that unlike MP and OMP, for which the extension to the complex field is straightforward, performed by simply replacing the transpose operator by the Hermitian operator, the extension of homotopy to the complex field is much more involved. To clarify the procedure for implementation, we summarise homotopy in Algorithm 1.

Considering an unconstrained optimisation problem

$$\min_{\boldsymbol{h}} \|\boldsymbol{r}-\boldsymbol{A}\boldsymbol{h}\|_2^2/2+\lambda\|\boldsymbol{h}\|_1 \tag{48}$$

the theory for penalty functions implies that homotopy starts at $\lambda \in \mathbb{R}$ large and $\boldsymbol{h}=0$ and terminates when $\lambda \to 0$. Meanwhile, $\boldsymbol{h}$ converges to the solution of noiseless sparse recovery problem

$$\min_{\boldsymbol{h}} \|\boldsymbol{h}\|_1 \quad \text{s.t.} \quad \boldsymbol{r}=\boldsymbol{A}\boldsymbol{h} \tag{49}$$

For the noisy sparse recovery problem as considered in this paper, the stopping condition $\lambda \to 0$ should be revised as

$$\|\boldsymbol{r}-\boldsymbol{A}\boldsymbol{h}\|_2 \leqslant \sigma_\eta \tag{50}$$

Suppose the objective function is

$$f_\lambda(\boldsymbol{h})=\|\boldsymbol{r}-\boldsymbol{A}\boldsymbol{h}\|_2^2/2+\lambda\|\boldsymbol{h}\|_1 \tag{51}$$

A necessary condition for $\boldsymbol{h}$ to be a minimiser of $f_\lambda(\boldsymbol{h})$ is that the zero vector is an element of the subdifferential of $f_\lambda(\boldsymbol{h})$, denoted as

$$\partial f_\lambda(\boldsymbol{h})=-\boldsymbol{A}^{\mathrm{H}}(\boldsymbol{r}-\boldsymbol{A}\boldsymbol{h})+\lambda\partial\|\boldsymbol{h}\|_1 \tag{52}$$

Algorithm 1. Complex homotopy

Step 0: Initialisation
$\boldsymbol{c}_0=\boldsymbol{A}^{\mathrm{H}}\boldsymbol{r}$, $\lambda_0=\max_{i\in\{1,\ldots,L\}}|c_0(i)|$;
$I_0=\arg\max_{i\in\{1,\ldots,L\}}|c_0(i)|$;
set both $\boldsymbol{h}_l\in\mathbb{C}^L$ and $\boldsymbol{d}_l\in\mathbb{C}^L$ to 0 vectors.

FOR $l=0,\ 1,\ \ldots,$

Step 1: Find the direction
solve $\boldsymbol{A}^{\mathrm{H}}(I_l)\boldsymbol{A}(I_l)\boldsymbol{d}_l(I_l)=\boldsymbol{c}_l(I_l)/\lambda_l$ and obtain $\boldsymbol{d}_l$;
set the components of $\boldsymbol{d}_l$ outside I_l to 0.

Step 2: Decide the step size
define $\boldsymbol{c}_l(I_l^c)=\boldsymbol{A}^{\mathrm{H}}(I_l^c)(\boldsymbol{r}-\boldsymbol{A}\boldsymbol{h}_l)$,
$d\boldsymbol{\mu}(I_l^c)=\boldsymbol{A}^{\mathrm{H}}(I_l^c)\boldsymbol{A}\boldsymbol{d}_l$;
FOR $i\in I_l^c$
  solve quadratic Equation (69);
EndFOR (i)
if $I_s\neq\varnothing$
  $\gamma_l^-=\min\{-\Re\{h_l(i)\}/\Re\{d_l(i)\},\ i\in I_s\}$
  $\gamma_l=\min\{\gamma_l^+,\gamma_l^-\}$
else
  $\gamma_l=\gamma_l^+$
end if
set $\boldsymbol{h}_{l+1}=\boldsymbol{h}_l+\gamma_l\boldsymbol{d}_l$ and $\lambda_{l+1}=\lambda_l-\gamma_l$;
set $\boldsymbol{c}_{l+1}(I_l)=(\lambda_l-\gamma_l)\boldsymbol{h}_l(I_l)/|\boldsymbol{h}_l(I_l)|$,
set $\boldsymbol{c}_{l+1}(I_l^c)=\boldsymbol{c}_l(I_l^c)-\gamma_l d\boldsymbol{\mu}(I_l^c)$.

Step 3: Update the selection
if $\gamma_l=\gamma_l^+$
  add a new column indicated by γ_l^+ into I_l and
  generate I_{l+1}
else
  delete the column indicated by γ_l^- from I_l and
  generate I_{l+1}
end if

Step 4: Check the stopping condition
if $\|\boldsymbol{r}-\boldsymbol{A}\boldsymbol{h}_{l+1}\|_2\leqslant\sigma_\eta$, quit the iteration;
otherwise continue ...

EndFOR (l)

where the subdifferential $\partial\|\boldsymbol{h}\|_1$ of $\|\boldsymbol{h}\|_1$ is given by

$$\partial\|\boldsymbol{h}\|_1=\left\{\boldsymbol{\omega}\in\mathbb{C}^L\ \middle|\ \begin{array}{ll}\boldsymbol{\omega}(i)=\frac{\boldsymbol{h}(i)}{|\boldsymbol{h}(i)|}, & \boldsymbol{h}(i)\neq 0\\ \boldsymbol{\omega}(i)=\{x\in\mathbb{C},|x|\leqslant 1\}, & \boldsymbol{h}(i)=0\end{array}\right\} \tag{53}$$

where $\boldsymbol{h}(i)$ and $\boldsymbol{\omega}(i)$ denote the ith component of $\boldsymbol{h}$ and $\boldsymbol{\omega}$, respectively. Let

$$T=\{i\ \mid \boldsymbol{h}(i)\neq 0\} \tag{54}$$

Trans. Emerging Tel. Tech. **23**:764–776 (2012)
DOI: 10.1002/ett

denote the support of $\boldsymbol{h}$ and

$$\boldsymbol{c} = \boldsymbol{A}^{\mathrm{H}}(\boldsymbol{r} - \boldsymbol{A}\boldsymbol{h}) \tag{55}$$

denote the correlations between the dictionary matrix and the residue. Then, the condition $0 \in \partial f_{\lambda}(\boldsymbol{h})$ can be written equivalently as two conditions

$$\boldsymbol{c}(T) = \lambda \cdot \frac{\boldsymbol{h}(T)}{|\boldsymbol{h}(T)|} \tag{56}$$

and

$$|\boldsymbol{c}(T^{\mathrm{c}})| \leqslant \lambda \tag{57}$$

where T^{c} stands for the complement of T. Homotopy traces a solution path by maintaining these two conditions.

To clarify the notation, we use subscript l to represent the parameters at the lth step. We initialise the parameters to be

$$\boldsymbol{c}_0 = \boldsymbol{A}^{\mathrm{H}}\boldsymbol{r} \tag{58}$$

$$\lambda_0 = \max_{i \in \{1,\ldots,L\}} |\boldsymbol{c}_0(i)| \tag{59}$$

$$I_0 = \arg \max_{i \in \{1,\ldots,L\}} |\boldsymbol{c}_0(i)| \tag{60}$$

At the lth step, an update direction $\boldsymbol{d}_l \in \mathbb{C}^L$ is first computed by solving

$$\boldsymbol{A}^{\mathrm{H}}(I_l)\boldsymbol{A}(I_l)\boldsymbol{d}_l(I_l) = \frac{\boldsymbol{c}_l(I_l)}{\lambda_l} \tag{61}$$

The components of $\boldsymbol{d}_l$ outside I_l are set to 0. Next, we figure out the step size γ_l so that a new solution at the $(l+1)$th step can be obtained as

$$\boldsymbol{h}_{l+1} = \boldsymbol{h}_l + \gamma_l \boldsymbol{d}_l \tag{62}$$

where $\boldsymbol{h}_l \in \mathbb{C}^L$ is initialised to be a zero vector and converges to the solution of Equation (48). We have

$$\begin{aligned} \boldsymbol{c}_{l+1} &= \boldsymbol{A}^{\mathrm{H}}(\boldsymbol{r} - \boldsymbol{A}\boldsymbol{h}_{l+1}) \\ &= \boldsymbol{A}^{\mathrm{H}}(\boldsymbol{r} - \boldsymbol{A}\boldsymbol{h}_l) - \gamma_l \boldsymbol{A}^{\mathrm{H}}\boldsymbol{A}\boldsymbol{d}_l \\ &= \boldsymbol{c}_l - \gamma_l \boldsymbol{A}^{\mathrm{H}}\boldsymbol{A}\boldsymbol{d}_l \end{aligned} \tag{63}$$

Because the current selected columns always follow Equation (56), we have

$$\boldsymbol{c}_{l+1}(I_l) = (\lambda_l - \gamma_l)\frac{\boldsymbol{h}_l(I_l)}{|\boldsymbol{h}_l(I_l)|} \tag{64}$$

On the other hand, we want to find a new column from I_l^c for the $(l+1)$th step,

$$\boldsymbol{c}_{l+1}(I_l^c) = \boldsymbol{c}_l(I_l^c) - \gamma_l d\boldsymbol{\mu}(I_l^c) \tag{65}$$

where we define

$$\boldsymbol{c}_l(I_l^c) \triangleq \boldsymbol{A}^H(I_l^c)(\boldsymbol{r} - \boldsymbol{A}\boldsymbol{h}_l) \tag{66}$$

$$d\boldsymbol{\mu}(I_l^c) \triangleq \boldsymbol{A}^H(I_l^c)\boldsymbol{A}\boldsymbol{d}_l \tag{67}$$

Once a column inside I_l^c appears to have the same projection as the columns inside I_l, which in fact occurs when Equation (64) equals Equation (65) in amplitude as

$$|\boldsymbol{c}_l(i) - \gamma_l d\boldsymbol{\mu}(i)| = \lambda_l - \gamma_l,\ i \in I_l^c \tag{68}$$

we consider it to be one possible candidate for the next selection because the residue can decline equally in this direction. We further define

$$c_R \triangleq \Re\{\boldsymbol{c}_l(i)\}, \quad c_I \triangleq \Im\{\boldsymbol{c}_l(i)\}$$

$$\mu_R \triangleq \Re\{d\boldsymbol{\mu}(i)\}, \quad \mu_I \triangleq \Im\{d\boldsymbol{\mu}(i)\}$$

and then obtain a quadratic equation as

$$\begin{aligned} &(\mu_R^2 + \mu_I^2 - 1)\gamma_l^2 \\ &+ 2(\lambda_l - c_R\mu_R - c_I\mu_I)\gamma_l + c_R^2 + c_I^2 - \lambda_l^2 = 0 \end{aligned} \tag{69}$$

We figure out two roots and select the smaller one, denoted as $\gamma(i), i \in I_l^c$, among which we obtain

$$\gamma_l^+ = \min_{i \in I_l^c}\{\gamma(i)\} \tag{70}$$

The other scenario leading to a breakpoint in the solution path occurs when one component of $\boldsymbol{h}_l(I_l)$ crosses 0, which means the real part and the imaginary part simultaneously equal 0. If

$$I_s = \left\{ \frac{\Re\{\boldsymbol{h}_l(i)\}}{\Re\{\boldsymbol{d}_l(i)\}} = \frac{\Im\{\boldsymbol{h}_l(i)\}}{\Im\{\boldsymbol{d}_l(i)\}}, i \in I_l \right\} \neq \varnothing \tag{71}$$

then

$$\gamma_l^- = \min_{i \in I_s}\left\{ -\frac{\Re\{\boldsymbol{h}_l(i)\}}{\Re\{\boldsymbol{d}_l(i)\}} \right\} \tag{72}$$

Finally, the step size is determined as

$$\gamma_l = \min\{\gamma_l^+, \gamma_l^-\} \tag{73}$$

We can use Equation (62) to update the solution $\boldsymbol{h}_{l+1}$. If $\gamma_l = \gamma_l^+$, we add a new column indicated by γ_l^+ into I_l and obtain I_{l+1}. If $\gamma_l = \gamma_l^-$, we delete the column indicated by γ_l^- from I_l and obtain I_{l+1}. We also update with

$$\lambda_{l+1} = \lambda_l - \gamma_l \tag{74}$$

These steps are repeated until the stopping condition (50) is satisfied.

The preceding extension to the complex field can be easily verified by forcing $c_I = 0$, $\mu_I = 0$ in Equation (69), which then reduces to the real-field form of homotopy [33]. Unlike OMP, where the whole projection is removed at each step, homotopy only removes part of it, which can be thought as a moderate greedy algorithm. Moreover, homotopy allows the columns to enter as well as to leave the current selection, which makes it more powerful than OMP.

5. SIMULATION RESULTS

The OFDM parameters used in our simulation are set according to [3], as listed in Table I.

Here, the values of N_{p} and N_{u} are different with those in [3] because we will compare the OFDM system and the wavelet system under the same conditions of bandwidth, duration, channel profile and data rate. The bandwidth $B = 12$ kHz is centred at $f_{\mathrm{c}} = 27$ kHz and divided into $N_{\mathrm{c}} = 512$ OFDM subcarriers, among which $N_{\mathrm{p}} = 70$ and $N_{\mathrm{u}} = 59$ are used for pilot subcarriers and null subcarriers, respectively. The useful length of each OFDM symbol is $T_{\mathrm{u}} = 42.67$ ms, which equals the reciprocal of the subcarrier spacing. The length of the zero padding guard interval is $T_{\mathrm{g}} = \tau_{\max} = 25$ ms or equivalently $N_{\mathrm{g}} = 300$ after sampling. Then, the length of each OFDM symbol is

$$T_{\mathrm{s}} = T_{\mathrm{u}} + T_{\mathrm{g}} = 67.67 \text{ ms}$$

We consider the UWA transmission in the unit of OFDM packet, with the same structure as in [3], which consists of one preamble, one postamble and 64 OFDM symbols, as shown in Figure 3. Both the preamble and the postamble are designed to be linear-frequency-modulated signals, which are used to mitigate the Doppler effect. Therefore, the Doppler scaling factor is regarded to be the same within each OFDM packet. The relative speed between the transmitter and the receiver is 8.3 knots, resulting in the Doppler shift at f_{c} to be around 76.98 Hz [3].

Table I. Orthogonal frequency-division multiplexing parameters.

Number of total subcarriers	$N_{\mathrm{c}} = 512$
Number of pilot subcarriers	$N_{\mathrm{p}} = 70$
Number of null subcarriers	$N_{\mathrm{u}} = 59$
Length of zero padding	$N_{\mathrm{g}} = 300$
Carrier frequency	$f_{\mathrm{c}} = 27$ kHz
Signal bandwidth	$B = 12$ kHz
Doppler shift at f_{c}	76.98 Hz

The multipath sparse channel model

$$h(\tau, t) = \sum_{i=1}^{S} a_i(t)\delta(\tau - \tau_i(t)) \tag{75}$$

which is introduced from [21], is used to generate UWA channel data. Within the OFDM packet, a different CIR vector is randomly generated for each OFDM symbol, according to the approach proposed in [36]. $\{a_i\} \sim \mathcal{CN}(\mathbf{0}, e^{-b\tau_i}\boldsymbol{I}_S)$. $b = 1/16$ is the exponential power delay profile, and τ_i is the delay spread for the ith path [36]. Here, we consider a five-path channel with the maximal channel delay spread $\tau_{\max} = 25$ ms. A zero CIR vector with the length L is first generated, where $S = 5$ positions are randomly selected as channel taps. Then, we produce $\{a_i\}$ as the attenuation for each path. We repeatedly generate a set of channel data for simulations. In practice, we may replace the aforementioned simulated channel data with the real UWA channel measurements, and it is verified in [21] that the simulations usually give the same performance trend as the real UWA experiments.

To fairly compare the channel estimation performance of OFDM and wavelet filter bank system, we set the length of wavelet packet the same as that of OFDM packet, as shown in Figure 3. The same preamble and postamble are employed. The parameters of the wavelet filter bank system are listed in Table II. The number of branches is supposed to be $M = 7$, and therefore, the length of each wavelet symbol is $N_{\mathrm{T}} = 2^{M-1} = 64$ or equivalently $T_{ws} = 2N_{\mathrm{T}}/B = 10.66$ ms. Because the number of total channel taps is $L_{\mathrm{w}} = B\tau_{\max}/2 = 150$, the training length $T_{\mathrm{wt}} = 35.67$ ms or equivalently $N_{\mathrm{wt}} = 214$ is enough to make accurate channel estimation. Then, the full data

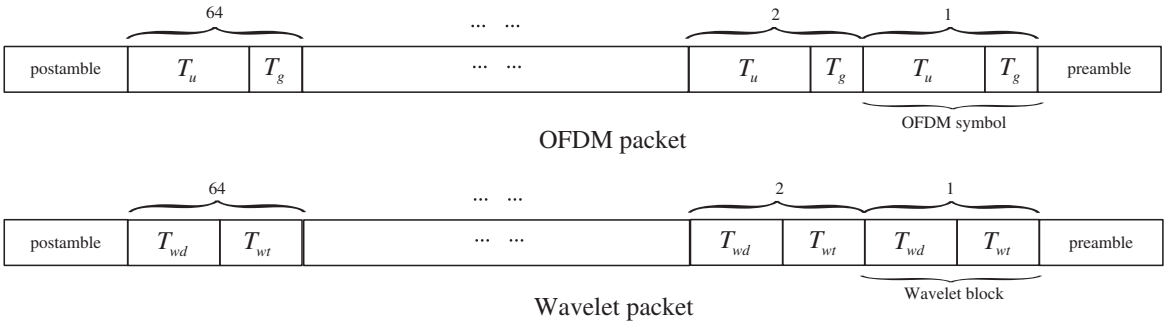

Figure 3. The structure of orthogonal frequency-division multiplexing (OFDM) packet and wavelet packet.

Trans. Emerging Tel. Tech. **23**:764–776 (2012)
DOI: 10.1002/ett

Table II. Parameters of wavelet filter bank system.

Number of branches in filter bank	$M = 7$
Length of each wavelet symbol	$N_T = 64$
Length of the training symbol	$N_{wt} = 214$
Length of the data symbols	$N_{wd} = 192$
Carrier frequency	$f_c = 27$ kHz
Signal bandwidth	$B = 12$ kHz
Doppler shift at f_c	76.98 Hz

length T_{wd} of each wavelet block is

$$T_{\mathrm{wd}} = T_s - T_{\mathrm{wt}} = 32\mathrm{ms}$$

or equivalently $N_{\mathrm{wd}} = 192$. We can figure out the number of wavelet data symbols in each wavelet block as follows:

$$N_{ws} = \left\lfloor \frac{T_{\mathrm{wd}}}{T_{ws}} \right\rfloor = 3$$

The data rate for OFDM and wavelet filter bank system is

$$R_{\mathrm{o}} = B \cdot \frac{T_{\mathrm{u}}}{T_{\mathrm{s}}} \cdot \frac{N_{\mathrm{c}} - N_{\mathrm{u}} - N_{\mathrm{p}}}{N_{\mathrm{c}}} = 5.67 \times 10^3 \ \text{(symbols per second)}$$

and

$$R_{\mathrm{w}} = B \cdot \frac{N_{ws} N_{\mathrm{T}}}{N_{\mathrm{wt}} + N_{\mathrm{wd}}} = 5.67 \times 10^3 \ \text{(symbols per second)}$$

respectively. Therefore, we compare two systems under the same conditions of bandwidth, duration, channel profile and data rate. The comparisons of the channel estimation performance in terms of MSE that is averaged over 64 OFDM symbols or 64 wavelet blocks are illustrated in Figure 4. It is observed that the MSE performance of the wavelet filter bank system is better than that of OFDM, especially for large signal-to-noise ratio (SNR), that is, SNR $>$ 20 dB. For the specific system, we also compare three different CS algorithms, including OMP, StOMP, which is an enhanced version of OMP [34], and the proposed homotopy. Here, we do not include the traditional LS method into our comparisons because LS works much worse than the sparse recovery algorithms when the pilot number is small [37]. In both systems, it is demonstrated that homotopy outperforms StOMP and OMP. Moreover, we verify our viewpoints through the bit error rate comparisons of two systems, as shown in Figure 5, where quadrature phase shift keying modulation is employed without channel coding.

To determine how many pilots or training sequences are needed to recover the sparse UWA channel to some required threshold MSE, we make a test of MSE comparisons with respect to different lengths of pilots or training sequences for OFDM and wavelet systems. As shown in Figure 6, the increase of pilots from 20 to 40 can mostly

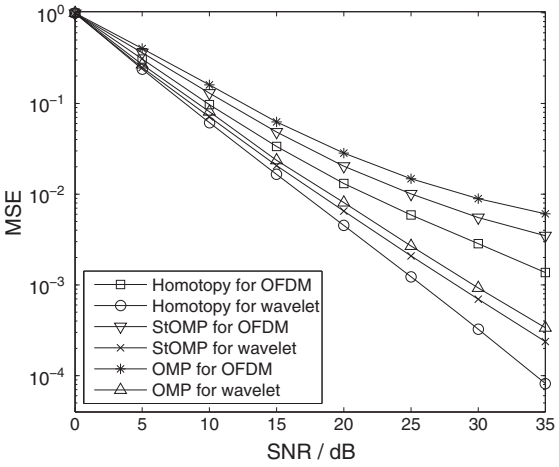

Figure 4. Comparisons of channel estimation for orthogonal frequency-division multiplexing (OFDM) and wavelet filter bank systems ($S = 5$). MSE, mean square error; OMP, orthogonal matching pursuit; SNR, signal-to-noise ratio; StOMP, stagewise orthogonal matching pursuit.

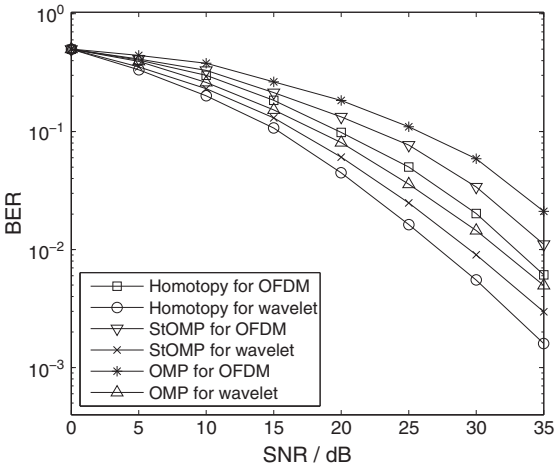

Figure 5. Bit error rate (BER) comparisons for orthogonal frequency-division multiplexing (OFDM) and wavelet filter bank systems ($S = 5$). OMP, orthogonal matching pursuit; SNR, signal-to-noise ratio; StOMP, stagewise orthogonal matching pursuit.

reduce the MSE; and the curve gets flat when it approaches 10^{-3}. So it is a reasonable trade-off to choose the length of pilots or training sequences between 60 and 80 while considering their nonnegligible overheads.

Additionally, we also change the number of channel multipath to $S = 20$, which treats the abundant multipath propagations in the UWA channel. The other parameters are kept the same. As shown in Figure 7, the performance of channel estimation for $S = 20$ is worse than that of $S = 5$, which implies that the sparser signals are much easier for the recovery. The wavelet filter bank system still outperforms OFDM. We also observe that homotopy is less

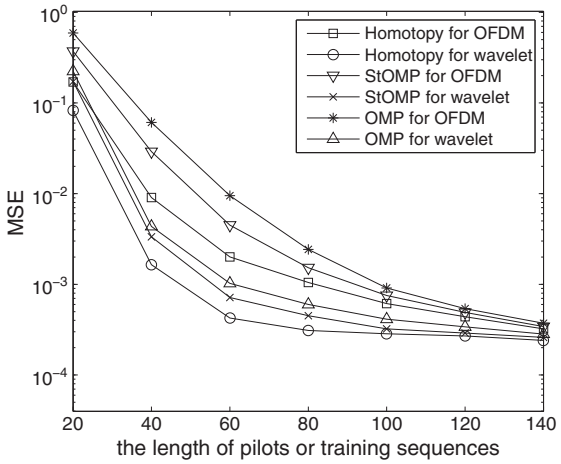

Figure 6. Mean square error (MSE) comparisons for different lengths of pilots or training sequences ($S = 5$). OFDM, orthogonal frequency-division multiplexing; OMP, orthogonal matching pursuit; StOMP, stagewise orthogonal matching pursuit.

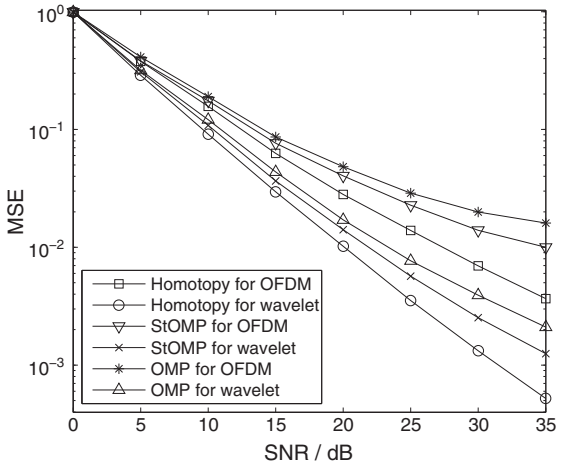

Figure 7. Comparisons of channel estimation for orthogonal frequency-division multiplexing (OFDM) and wavelet filter bank systems ($S = 20$). MSE, mean square error; OMP, orthogonal matching pursuit; SNR, signal-to-noise ratio; StOMP, stagewise orthogonal matching pursuit.

Table III. Running times of different compressed sensing algorithms.

	CPU time (s)	
Algorithm type	OFDM	Wavelet filter bank system
Homotopy	0.876	0.584
StOMP	1.211	0.983
OMP	0.849	0.539

CPU, central processing unit; OFDM, orthogonal frequency-division multiplexing; OMP, orthogonal matching pursuit; StOMP, stagewise orthogonal matching pursuit.

influenced by the change of the sparsity than StOMP and OMP, which demonstrates the robustness of the proposed homotopy algorithm.

The complexities of the OMP, StOMP and homotopy algorithm for two systems in terms of the central processing unit running time are compared in Table III where SNR is fixed at 30 dB and $S = 20$. The experiments are performed using MATLAB v7.9 (R2009b) running on a Lenovo laptop with an Intel Core 2 Duo central processing unit at 2.5 GHz and 2 GB of memory. We notice that the running time of StOMP is much larger than that of OMP and homotopy, whereas the running time of homotopy is similar to that of OMP. Moreover, the speed of sparse recovery for the wavelet filter bank system is much faster than that for the OFDM system. The reason lies in the different sizes of the measurement matrix in two systems, which directly determines the searching time of two algorithms. In OFDM system, we use $N_{\mathrm{p}} = 70$ pilots to reconstruct the sparse UWA channel, where $S = 20$ channel taps of a total of $N_{\mathrm{g}} = 300$ taps are nonzero and the size of the measurement matrix is 70 by 300. In the wavelet filter bank system, we use $N_{\mathrm{wt}} - L_{\omega} + 1 = 65$ training symbols to reconstruct the UWA channel where $S = 20$ of only $L_{\mathrm{w}} = 150$ channel taps are nonzero. The size of the measurement matrix is only 65 by 150, which is much slimmer than that of OFDM.

6. CONCLUSION

In this paper, we have proposed a wavelet filter bank system as the extension of the OFDM system for UWA communications. We have exploited the convolutional structure and formulated the pilot-assisted UWA channel estimation as a sparse recovery problem. We have investigated the RIP of the measurement matrix via eigenvalue analysis and the Gershgorin circle theorem and proved that it satisfied RIP. We have also proposed a low-complexity complex-field homotopy algorithm for sparse channel estimation regarding the fact that in practice the channel taps of each path are usually complex valued. Simulation results show that the wavelet filter bank system achieves more accurate UWA channel estimation performance than the OFDM system under the same conditions of bandwidth, duration, data rate and channel profile. The proposed complex homotopy algorithm outperforms StOMP and OMP in both systems whereas its computational complexity is similar to OMP. Because this work is based on the ICI-ignorant receiver, future work will continue to explore the more complicated ICI-aware receivers [21], as well as other low-complexity CS algorithms and the possible trade-off between the data rate and the channel estimation accuracy.

ACKNOWLEDGEMENTS

The authors would like to thank Prof. Xiaodong Wang of Columbia University for his helpful comments and suggestions. The work is supported by the National Natural

Science Foundation of China (NSFC) under grant 60872075, the Scientific Research Foundation of Southeast University under grant Seucx201116 and the Huawei Innovative Research Plan and CAST 8804009011.

REFERENCES

1. Stojanovic M, Preisig J. Underwater acoustic communication channels: propagation models and statistical characterization. *IEEE Communications Magazine* 2009; **47**(1): 84–89.
2. Sharif BS, Neasham J, Hinton OR, Adams AE. A computationally efficient Doppler compensation system for underwater acoustic communications. *IEEE Journal of Oceanic Engineering* 2000; **25**(1): 52–61.
3. Li B, Zhou S, Stojanovic M, Freitag L, Willett P. Multicarrier communication over underwater acoustic channels with nonuniform Doppler shifts. *IEEE Journal of Oceanic Engineering* 2008; **33**(2): 198–209.
4. Kang T, Iltis RA. Iterative carrier frequency offset and channel estimation for underwater acoustic OFDM systems. *IEEE Journal on Selected Areas in Communications* 2008; **26**(9): 1650–1661.
5. Ou H, Allen J, Syrmos V. Frame-based time-scale filters for underwater acoustic noise reduction. *IEEE Journal of Oceanic Engineering* 2011; **36**(2): 285–297.
6. Lottici V, Reggiannini R, Carta M. Pilot-aided carrier frequency estimation for filter-bank multicarrier wireless communications on doubly-selective channels. *IEEE Transactions on Signal Processing* 2010; **58**(5): 2783–2794.
7. Yu L, White LB. Optimum receiver design for broadband Doppler compensation in multipath/Doppler channels with rational orthogonal wavelet signaling. *IEEE Transactions on Signal Processing* 2007; **55**(8): 4091–4103.
8. Mittal V, Gautam Y, Mallik R, Joshi S. Analysis of wavelet modulation in frequency-selective fading. *IEEE Transactions on Vehicular Technology* 2007; **56**(6): 3818–3826.
9. Lakshmanan MK, Nikookar H. A review of wavelets for digital wireless communication. *Wireless Personal Communications* 2006; **37**(3): 387–420.
10. Chen S, Dai G, Rao W. ICI mitigation and diversity gain for OFDM systems in time-varying multipath fading channels. *European Transactions on Telecommunications* 2011; **22**(2): 61–67.
11. Baig S, Mughal HJ. Multirate signal processing techniques for high-speed communication over power lines. *IEEE Communications Magazine* 2009; **47**(1): 70–76.
12. Hirakawa K, Wolfe P. Rewiring filter banks for local Fourier analysis: theory and practice. *IEEE Transactions on Information Theory* 2011; **57**(8): 5360–5374.
13. Donoho DL. Compressed sensing. *IEEE Transactions on Information Theory* 2006; **52**(4): 1289–1306.
14. Benedetto S, Caire G, Koetter R, Urbanke R. New directions in information theory. *European Transactions on Telecommunications* 2008; **19**(4): 329–332.
15. Baraniuk R, Candes E, Elad M, Ma Y. Applications of sparse representation and compressive sensing. *Proceedings of the IEEE* 2010; **98**(6): 906–909.
16. Bajwa WU, Haupt J, Sayeed AM, Nowak R. Compressed channel sensing: a new approach to estimating sparse multipath channels. *Proceedings of the IEEE* 2010; **98**(6): 1058–1076.
17. Berger CR, Wang Z, Huang J, Zhou S. Application of compressive sensing to sparse channel estimation. *IEEE Communications Magazine* 2010; **48**(11): 164–174.
18. Kang T, Iltis RA. Matching pursuits channel estimation for an underwater acoustic OFDM modem. In *Proceedings of the IEEE International Conference on Acoustics, Speech and Signal Processing (ICASSP 2008)*, Las Vegas, NV, USA, 2008; 5296–5299.
19. Josso NF, Zhang JJ, Fertonani D, Papandreou-Suppappola A, Duman TM. Time-varying wideband underwater acoustic channel estimation for OFDM communications. In *Proceedings of the IEEE International Conference on Acoustics, Speech and Signal Processing (ICASSP 2010)*, Dallas, TX, USA, 2010; 5226–5629.
20. Li W, Preisig JC. Estimation of rapidly time-varying sparse channels. *IEEE Journal of Oceanic Engineering* 2007; **32**(4): 927–939.
21. Berger CR, Zhou S, Preisig JC, Willett P. Sparse channel estimation for multicarrier underwater acoustic communication: from subspace methods to compressed sensing. *IEEE Transactions on Signal Processing* 2010; **58**(3): 1708–1721.
22. Huang JZ, Berger CR, Zhou S, Huang J. Comparison of basis pursuit algorithms for sparse channel estimation in underwater acoustic OFDM. In *Proceedings of the MTS/IEEE OCEANS Conference*, Sydney, Australia, 2010; 1–6.
23. Mason SF, Berger CR, Zhou S, Willett P. Detection, synchronization, and Doppler scale estimation with multicarrier waveforms in underwater acoustic communication. *IEEE Journal on Selected Areas in Communications* 2008; **26**(9): 1638–1649.
24. Khairy MM. A novel frequency offset estimation technique for mobile WiMAX. *European Transactions on Telecommunications* 2011; **22**(1): 45–50.
25. Bianchi T, Argenti F, Re E. Performance of filter bank and wavelet transceivers in the presence of carrier frequency offset. *IEEE Transactions on Communications* 2005; **53**(8): 1323–1332.
26. Candes EJ, Tao T. Decoding by linear programming. *IEEE Transactions on Information Theory* 2005; **51**(12): 4203–4215.

27. Haupt GRJ, Bajwa WU, Nowak R. Toeplitz compressed sensing matrices with applications to sparse channel estimation. *IEEE Transactions on Information Theory* 2010; **56**(11): 5862–5875.
28. Tropp JA. Just relax: convex programming methods for identifying sparse signals in noise. *IEEE Transactions on Information Theory* 2006; **52**(3): 1030–1051.
29. Wright SJ, Nowak RD, Figueiredo MAT. Sparse reconstruction by separable approximation. *IEEE Transactions on Signal Processing* 2009; **57**(7): 2479–2493.
30. Tropp JA, Gilbert AC. Signal recovery from random measurements via orthogonal matching pursuit. *IEEE Transactions on Information Theory* 2007; **53**(12): 4655–4666.
31. Dai W, Milenkovic O. Subspace pursuit for compressive sensing signal reconstruction. *IEEE Transactions on Information Theory* 2009; **55**(5): 2230–2249.
32. Figueiredo M, Nowak R, Wright S. Gradient projection for sparse reconstruction: application to compressed sensing and other inverse problems. *IEEE Journal of Selected Topics in Signal Processing* 2007; **1**(4): 586–597.
33. Donoho DL, Tsaig Y. Fast solution of ℓ_1-norm minimization problems when the solution may be sparse. *IEEE Transactions on Information Theory* 2008; **54**(11): 4798–4812.
34. Donoho DL, Tsaig Y, Drori I, Starck J-C. Sparse solution of underdetermined linear equations by stagewise orthogonal matching pursuit 2006. Available from: http://www.cs.tau.ac.il/ idrori/StOMP.pdf.
35. Efron B, Hastie T, Johnstone I, Tibshirani R. Least angle regression. *Annals of Statistics* 2004; **32**(2): 407–499.
36. Raghavendra MR, Giridhar K. Improving channel estimation in OFDM systems for sparse multipath channels. *IEEE Signal Processing Letters* 2005; **12**(1): 52–55.
37. Qi C, Wu L. A hybrid compressed sensing algorithm for sparse channel estimation in MIMO OFDM systems, In *Proceedings of the IEEE International Conference on Acoustics, Speech and Signal Processing (ICASSP 2011)*, Prague, Czech Republic, 2011; 3488–3491.

Trans. Emerging Tel. Tech. **23**:764–776 (2012) © 2012 John Wiley & Sons, Ltd.
DOI: 10.1002/ett